Machining of additively manufactured alloy 718 in as-built and heat-treated condition: surface integrity and cutting tool wear

The International Journal of Advanced Manufacturing Technology (2024) 130:1823–1842
https://doi.org/10.1007/s00170-023-12727-w

ORIGINAL ARTICLE

Machining of additively manufactured alloy 718 in as-built and heat-treated condition: surface integrity and cutting tool wear

Jonas Holmberg[1] · Johan Berglund[1] · Ulrika Brohede[2] · Pia Åkerfeldt[3] · Viktor Sandell[3] · Amir Rashid[4] · Xiaoyu Zhao[4] · Sasan Dadbakhsh[4] · Marie Fischer[5] · Eduard Hryha[5] · Urban Wiklund[6] · Carl Johan Karlsson Hassila[6] · Seyed Hosseini[1]

Received: 4 August 2023 / Accepted: 23 November 2023 / Published online: 14 December 2023

Abstract
Additive manufacturing (AM) using powder bed fusion is becoming a mature technology that offers great possibilities and design freedom for manufacturing of near net shape components. However, for many gas turbine and aerospace applications, machining is still required, which motivates further research on the machinability and work piece integrity of additive-manufactured superalloys. In this work, turning tests have been performed on components made with both Powder Bed Fusion for Laser Beam (PBF-LB) and Electron Beam (PBF-EB) in as-built and heat-treated conditions. The two AM processes and the respective heat-treatments have generated different microstructural features that have a great impact on both the tool wear and the work piece surface integrity. The results show that the PBF-EB components have relatively lower geometrical accuracy, a rough surface topography, a coarse microstructure with hard precipitates and low residual stresses after printing. Turning of the PBF-EB material results in high cutting tool wear, which induces moderate tensile surface stresses that are balanced by deep compressive stresses and a superficial deformed surface that is greater for the heat-treated material. In comparison, the PBF-LB components have a higher geometrical accuracy, a relatively smooth topography and a fine microstructure, but with high tensile stresses after printing. Machining of PBF-LB material resulted in higher tool wear for the heat-treated material, increase of 49%, and significantly higher tensile surface stresses followed by shallower compressive stresses below the surface compared to the PBF-EB materials, but with no superficially deformed surface. It is further observed an 87% higher tool wear for PBF-EB in as-built condition and 43% in the heat-treated condition compared to the PBF-LB material. These results show that the selection of cutting tools and cutting settings are critical, which requires the development of suitable machining parameters that are designed for the microstructure of the material.

Keywords Additive manufacturing · Alloy 718 · Machining · Tool wear · Surface integrity

✉ Jonas Holmberg
jonas.holmberg@ri.se

[1] Department of Manufacturing Processes, RISE Research Institutes of Sweden AB, Argongatan 30, Mölndal, Sweden

[2] Department of Production Technology, Swerim AB, Isafjordsgatan 28A, Kista, Sweden

[3] Division of Material Science, Luleå University of Technology, 971 87 Luleå, Sweden

[4] Department of Production Engineering, KTH Royal Institute of Technology, Brinellvägen 68, Stockholm, Sweden

[5] Department of Industrial and Materials Science, Chalmers University of Technology, Hörsalsvägen 7B, Göteborg, Sweden

[6] Department of Material Science, Ångströmlaboratoriet, Uppsala University, Lägerhyddsvägen 1, Uppsala, Sweden

1 Introduction

Additive manufacturing (AM) using powder bed fusion is becoming a mature technology that enables major weight reduction, material waste reduction and smart component design that enables a disrupted supply chain. Metal additive manufacturing allows for a flexible production but requires further development to become a robust zero-defect manufacturing method where the final part is near net shape. This requires better control of all steps in the manufacturing chain, from the selection of powder feedstock and AM fabrication method, through the post-AM treatment, to finishing the part [1]. The mentioned motives promote powder bed AM for gas turbine and aerospace applications of nickel-based superalloys [2]. For many aero engine components,

the process route involves costly and time-consuming machining of these difficult-to-machine superalloys, which stands for the majority of the material grade for the parts of the engine's hot section. Using AM for such an application would therefore require much less machining compared to the conventional process route. Difficulties of machining superalloy 718 are mainly due to its prone to deformation hardening and kept mechanical strength at elevated temperatures, which is resulting in high cutting forces and tool wear [3]. Hence, utilising additive manufacturing ability for near the final component shape and optimising the machining operation is highly attractive from an industrial point of view. The majority of the research on the AM of alloy 718 is focusing on how to optimize the mechanical properties of the as-built parts through material and process development [4–7]. As metal AM has become more mature, the application areas have extended to demanding and critical components, why post-processes involving the machining of additively manufactured materials become important to reach the required tolerances [4]. Especially suitable for such applications are the Powder Bed Fusion Laser Beam (PBF-LB) and Electron Beam (PBF-EB) process, further described elsewhere [8, 9]. The mechanical performance could be enhanced by machining as shown by Hatami et al. for PBF-LB 316L, which improved both topography and introduced compressive residual stresses [10].

The anisotropic microstructure of AM materials is one major difference from conventionally manufactured alloy 718. However, awareness of this may be used to optimize the directional dependence based on the load in service for the final application. As shown by Wimler et al. and Deng et al., the AM part could have enhanced material properties in one orientation but inferior in the other direction [11, 12]. The degree of this orientation dependence is given by the printing process (PBF-LB, PBF-EB, etc.), as such, and is closely related to how the printing is set up and how the material solidifies after melting [4, 13]. The as-built microstructure (grain size, texture, precipitates amount, size and distribution) will have a direct impact on the machinability and mechanical properties. Currently, there are no general strategies to optimize the machining and mechanical properties in the design phase. It is therefore a great risk involved when recommended machining settings for conventional materials are used, which can result in inferior surface integrity and enhanced tool wear. Additionally, the amount of material to be printed does not allow for extensive experimental investigations; hence, "first-time-right" becomes even more critical. These challenges prompt the development of innovative methods to identify the process window for machining of the commercially available AM alloys, maintaining machined surface characteristics and dimensional tolerances. As discussed by Stavropoulos et al. [14], the need for subtractive post processing methods for AM is obvious, and future trends move towards hybrid machines, which include cells of robotic post processing machinery.

Machining of AM materials mainly covers the turning of Ti-6Al-4 V and is well described in the comprehensive work by Zhang et al. [15], but there is a growing interest of machining performance of other methods and materials such as alloy 718. The main concern when machining AM materials is the unpredictable tool wear due to the anisotropic microstructure of AM material, which in turn determines the surface integrity of the work piece. The majority of the current literature regarding the machining of AM nickel-based alloys covers reports of alloy 625 [16–19]. However, alloy 625 has lower thermal conductivity and lower hardness compared to alloy 718, which generally makes it easier to machine, also proved by Parida et al. [20]. Relevant fundamental work on alloy 718 was presented by Malakizadi et al. [21] who compared the influence from the microstructure on the tool wear of PBF-LB and PBF-EB. It was shown that the texture from printing and material work hardening prior to chip breaking significantly influenced the cutting forces. Evidently, a higher cutting force was registered for the PBF-EB material due to the stronger texture. Additionally, larger cutting tool wear was observed for the PBF-EB material due to a higher amount of hard oxide inclusions compared to the PBF-LB material. Peréz-Ruiz et al. confirmed the influence from texture on cutting forces in the milling of PBF-LB components [22]. It was shown that the directional dependency of the milling force is closely related to the interaction between the orientation of the plane of the shear band (due to the relative tool position with respect to the work piece), predominant crystalline textures, orientation and size of the PBF-LB-printed columnar grains. In the work by Chen et al., the machining performance of PBF-LB and wrought alloy 718 was compared with turning using a coated cemented carbide tool [23]. It was concluded that cutting force and temperature were lower for the PBF-LB material compared to the wrought material. The tool wear was also much lower for the PBF-LB material. A great influence of different laser printing parameters, mainly affecting the surface region microstructure and porosity, on topography and deformation after finish slot milling using a solid end mill was shown in the works by Taşcıoğlu et al. [24]. Kaynak et al. also disclosed how to improve the surface roughness when finish milling PBF-LB alloy 718 by using a low feed rate [25].

As observed by several authors, the machining of AM materials is mainly affected by abrasion and adhesion as the main wear mechanisms [21, 23, 26]. The review by Bartolomeis et al. on the machinability of AM alloy 718 generally concluded that the lower hardness and higher ductility together with the smaller dimensions of the carbides of AM material will promote a reduction of abrasive wear of the cutting tool [27]. The review also mentioned the problem associated with anisotropy related to the

building direction which involves a variation in the thermomechanical loads of the cutting tools. This may require the use of cutting tools with higher toughness or develop new grades suitable for AM considering the microstructure variations.

Generic learning of the response of machining in AM material was shown by Zhao et al. who investigated the effects of superficial defects on the as-built surface of PBF-EB alloy 718 [7]. It was observed a significantly lower material strength after shallow milling of the rough outer surface compared to a deeper milled surface, which was due to surface defects. A similar trend was observed for PBF-LB Ti-6Al-4 V by Oyelola et al. [28]. As the tools wear out, unpredictable tool damages may occur which could result in damages as shown by Yang et al. [19].

In respect to conventionally manufactured nickel-based superalloys, machinability is mainly related to the materials prone to work hardening, which alters the cutting conditions [29]. Arunachalam et al. exemplified this in an investigation of the cutting performance of conventional alloy 718 using different tools and parameters [30]. It was shown that a round-coated carbide tool may induce desirable compressive stresses for specific settings and that flank wear and notching were the most common failure mechanisms involved. Jinal et al. suggested to use TiAlN-coated inserts since they showed the highest performance [31]. Other researchers have also concluded that notch wear is the predominant tool wear due to the work hardening of conventional alloy 718 [3, 32]. It is therefore suggested to use a large side cutting edge angle and a negative rake angle. It is also suggested to increase the nose angle to increase the tool-chip contact area and thereby promote an improved tool strength and a prolonged tool life. Flank wear and chipping are also common but instead related to diffusion or abrasive wear mechanisms, due to the thermal and mechanical loading fatigue of the tools. Controlling the tool wear is essential as it determines the induced residual stresses in the work piece material as shown by Sharman for turning in conventional Inconel 718 [33]. This is a consequence of a change of the cutting tool-work piece contact as the cutting edge wears out, which in turn will redistribute the loads during cutting.

The main difference with AM compared to conventional material is the gradually varying microstructure from the surface to the core. This microstructural texture is generated in the printing, which may alter both the amount and distribution of precipitates, but also in the grain size and anisotropy. For conventionally manufactured wrought alloy 718, Olovsjö et al. showed that larger grain size resulted in higher notch wear and a greater deformation depth [34]. The induced stress in the work piece is a balance between the thermal and mechanical load on the tool. Tensile stresses are induced as the temperature rises on the clearance side, while as the cutting forces increase the stresses become compressive as shown by Madariaga et al. [35].

For most AM parts, a subsequent heat treatment is required in order to relieve residual stresses, to minimize the pores (Hot Isostatic Press) and to improve the mechanical properties. Deng et al. investigated the impact of heat treatment for PBF-LB alloy 718, which significantly increased the material strength but decreased the ductility [12]. It was also shown that the directional difference of the as-built material decreased with increasing heat treatment temperature as the residual stresses and dislocations decreased. Tucho et al. showed apart from stress relieving, that heat treatment resulted in grain coarsening of PBF-LB alloy 718 [5]. However, both the stresses and microstructure will have a direct effect on the machinability as shown by Careri et al. [36].

Based on previous work in the existing literature, there is a substantive amount of research reporting on the influence of the different microstructure constituents in s components compared to conventionally manufactured parts in terms of (1) different phase volumes, (2) different precipitates and dislocation networks, (3) different grain sizes, microstructure anisotropy, etc. Further, it is also shown in some cases, even after heat treatment, that the microstructure still maintains some characteristics that cannot be found in conventionally manufactured materials. Additionally, the topography, residual stresses and microstructure, is often deficient and faces problems with distortion when separated from the building plates. Therefore, for almost all functional and mating surfaces, subtractive operations are needed to reach the high dimensional accuracies and tolerances. Given the high accumulated value of AM parts, from design to build times, in combination with a relatively low machining tool cost, there is less focus on the machining of AM parts. However, a tool breakage could be a potentially large cost for machined AM parts, if the component needs to be scrapped. Also, due to a lack of knowledge of proper machining strategies for these parts, tool selection and local variation of material properties, there are obvious risks of manufacturing surfaces with inferior properties. The objective of this work is to identify the risks, in regard to tool wear and workpiece surface integrity, when applying conventional cutting parameters in the machining of Alloy 718 manufactured with PBF-LB and PBF-EB.

2 Experimental procedure

2.1 Precursor material and heat-treatment

The virgin and gas-atomised IN718 powders used for the studied processes, PBF-LB and PBF-EB, were supplied by Höganäs Sweden AB. The chemical composition of the

powder, AMPERPRINT®, is shown in Table 1. The precursor material for the PBF-LB process with nearly spherical particles ranged from 18 to 50 µm, with a D50 of 30 µm. This can be compared to the spherical particles as used for the PBF-EB, which had a D50 of 71 µm.

Tubular test samples were manufactured with the following design dimensions: length of 110 mm, outer diameter of 90 mm and wall thickness of 10 mm. The build direction was along the symmetry axis of the tubular samples. An internal lattice structure was used to improve the strength and to reduce distortion caused by the repeating heating and cooling during the printing process.

Two out of five samples from each manufacturing process were subjected to heat treatment according to the AMS-5662 standard, designed for wrought Alloy 718. The heat treatment cycle included a solution treatment at 970 ℃ for 60 min, followed by two ageing treatments at 718 ℃ for 480 min and 621 ℃ for 480 min and finally cooled in air to ambient temperature.

2.2 Laser-based powder bed fusion (PBF-LB)

The five PBF-LB samples were printed using an EOS M290 machine that uses a 400-W Yb (Ytterbrium) fiber laser operating at a wavelength of 1060–1100 nm and an F-Theta focusing lens; the focal length of the F-Theta lens is 410 mm. Printing was done using settings supplied by the machine manufacturer for alloy 718, default process parameters ID: IN718_Performance M291.2.11. This was carried out by using a layer thickness of 40 µm and a "stripe" scanning strategy with a 67° rotation between each layer consisting of an optimized sequence of in-fill and contour scanning, with the latter ensuring dimensional accuracy and good surface properties. To prevent excessive oxidation and part distortion during manufacturing, argon gas with a 4.6 purity was used. The process atmosphere during printing is established by flushing the build chamber by argon until a stable oxygen level of 0.1% O_2 is reached [37]. After manufacturing, the parts were removed from the build plate using wire electrical discharge machining.

2.3 Electron beam powder bed fusion (PBF-EB)

The five PBF-EB samples were printed in an Arcam A2X_EBM machine (Arcam EBM, a GE Additive company) with a 3 kW tungsten filament-based gun operating under a high working temperature of 1025 °C in vacuum. A high accelerating voltage of 60 kV was applied to generate the electron beam. For each layer, the default parameters from the machine manufacturer were used for this material using the build-plate with the dimensions 200 × 200 mm. Each slice was melted using a commercial multi-beam contouring strategy, having a starting hatching angle of 0° and a rotation angle of 96.5° per layer. The main process parameters for the contour and the hatch region are provided in Table 2. It should be noted that the automatic mode was on during EBM. This could also adjust the parameters according to each layer cross-section to keep the melting consistent for different part geometries. Upon completion, the solid 3D part, along with the unmelted powder, slowly cooled down to about 50 °C after which the build was removed from the machine and cleaned of the sintered powder using an Arcam powder recovery system. In total, 5 samples as-built were produced with the PBF-EB process (see Fig. 1B).

2.4 Machining

The turning tests were performed in a CNC Okuma LB300-M lathe. The samples were asymmetrical and difficult to machine; hence, a fixture was created as well as a 45° chamfer to enable a stable tool entry and eliminate the risk of tool failure (see Fig. 2). The machining test was done in two steps: step 1, roughing to remove the asymmetry; and step 2, a cutting test to study surface integrity after machining and the associated tool wear. Step 1, also referred to as "cleaning cut," involved 3 cutting passes in the as-printed condition and 2 cutting passes in the heat-treated condition with the

Table 1 Chemical composition of the precursor powder granules for the PBF-LB and PBF-EB processes. Values are given in wt.%, from powder certificate of AMPERPRINT® Höganäs Sweden AB

Ni	Cr	Nb	Mo	Ti	Al	C	B	N	O	P	S	Cu/Mn/Si
53.8	19	5.4	3	1	0.5	0.04	< 0.002	0.012	0.01	< 0.005	0.002	< 0.01

Table 2 Process parameters for the PBF-EB printing, *O, outer; *I, inner

Scanning strategy	Order	Beam speed (mm/s)	Beam current (mA)	Spacing offset (mm)
Contour	Inner to outer	540^{*O}, 1000^{*I}	$8^{*O, *I}$	0.3^{*O}, 0.2^{*I}
Hatch	End with hatching	4530	15	0.125

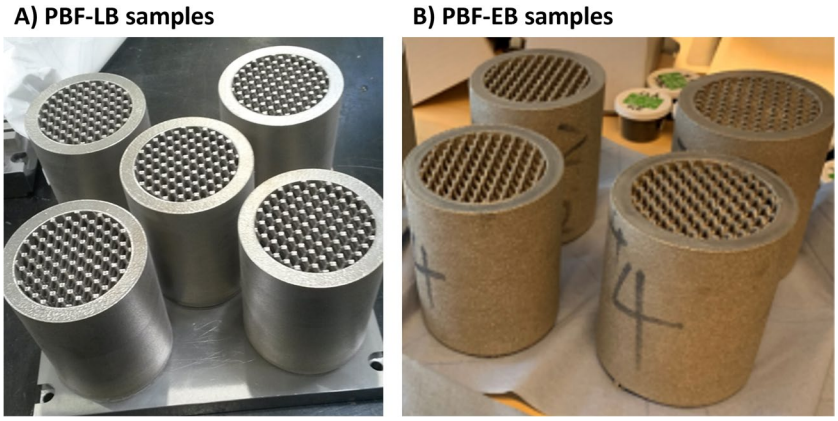

Fig. 1 Printed test objects from the PBF-LB (**A**) and PBF-EB (**B**) process as examined here

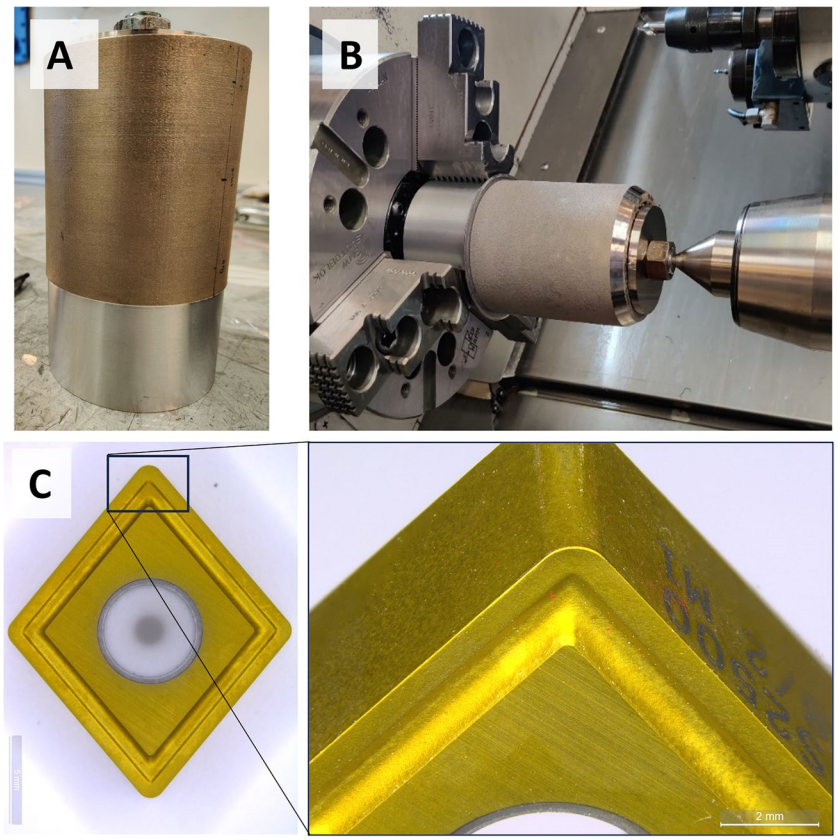

Fig. 2 Overview of the turning test sample clamping design (**A**), set-up in the lathe (**B**), and overview of the insert used for the turning tests (**C**)

same cutting parameters as the subsequent cutting test. The cutting test in step 2, also referred to as finishing, was done using a new cutting tool for each cutting pass.

Machining parameters, used for both "cleaning cuts" and cutting tests, selected on the tool manufacturer's recommendation for conventional alloy 718 and with the target to remove the least amount of material until a cleaned surface is achieved: cutting speed (v_c) 70 m/min, feed rate (f) 0.075 mm/rev, and depth of cut (a_p) 0.3 mm. All machining tests were conducted with flood coolant. As cutting tools, the PVD-coated carbide inserts ISO CNMG 12 0408–TS2500 were used, with geometry as seen in Fig. 2 and a corner radius of 0.8 mm, clearance angle of 0° and edge radius of approximately 32 ± 2 µm, as measured for a new insert. Table 3 shows the test matrix that was used in this study. The purpose of the clean cut was to secure continuous cutting conditions during the cutting test.

2.5 Surface integrity evaluation

2.5.1 Surface topography and part geometry

The rough nature of the surface in the as-built condition is challenging to assess, which is why we implement the

Table 3 Turning test matrix and cutting length

Printing	Sequence	Condition	Insert	Machining length (mm)	# Cut	CCL (m)
PBF-LB	Cleaning	As-built	C1	90	1	339
				90	2	676
				90	3	1011
	Pass 1		S1	90	4	335
	Pass 2		S2	85	5	626
	Pass 3—finish		S3	80	6	868
	Cleaning	Heat treated	C2	90	1	339
				90	2	676
	Pass 1		S4	90	3	335
	Pass 2		S5	85	4	626
	Pass 3—finish		S6	80	5	868
PBF-EB	Cleaning	As-built	C3	90	1	339
				90	2	676
				90	3	1011
	Pass 1		E1	90	4	335
	Pass 2		E2	85	5	626
	Pass 3—finish		E3	80	6	868
	Cleaning	Heat treated	C4	90	1	339
				90	2	676
	Pass 1		E4	90	3	335
	Pass 2		E5	85	4	626
	Pass 3—finish		E6	80	5	868

strategy described by Townsend et al. [38] and the confocal fusion technique as described by Flys et al. [39]. The measurements were performed with a Sensofar S Neox instrument with a × 20 magnification resulting in a lateral resolution of 1.29 µm measuring an area of 2 × 2 mm. In this work, the surfaces are characterized using Sa (arithmetic mean height), S10z (ten-point height) and Sdr (developed interfacial area ratio) from the ISO 25178–2:2012 standard [40]. The measured data were processed by applying a 2nd degree polynomial fit for form removal followed by filtering using a spatial median noise-reduction filter, with a window size of 5 × 5 points, to reduce short wavelengths, producing S-F data sets for analysis.

The sample distortion was measured with an optical scanner, GOM ATOS using a measurement volume of 320 × 240 × 240 mm and a point spacing of 0.104 mm, which successively added data from different incident angles giving a resulting spatial resolution of < 10 µm. The evaluation of the samples was performed with ATOS Professional 2018 software with the CAD model and by fitting an ideal cylinder to the measured data to calculate the component cylindricity and roundness [41]. The cylindricity was calculated as the form deviation from an ideal cylinder and the roundness as the deviation from a perfect circle along the height of the part.

2.5.2 Microstructure and hardness

The material characterisation in terms of porosity, hardness and microstructure was evaluated on cross sections in a direction along the build direction for test specimens of each sample. The cross sections were prepared by grinding and polishing in steps using sample preparation techniques suitable for superalloys until the final Oxide Polishing Suspension (OPS) polishing. The cross-section surface profile topography was analysed from images produced by an optical microscope (Nikon Eclipse MA200) in 100 × magnification. The porosity was evaluated on the same cross-sections using an image analysis software MIPAR (v.3.0.3). The porosity was evaluated using image analysis based on segmentation of the images using Otsu's thresholding method of the grayscale values. Pores with the largest dimension smaller than 5 µm were disregarded. The shape of each segmented porosity was then classified as spherical or irregular using an eccentricity measure in MIPAR where pores with values > 0.85 were considered irregular. The analysed area was in the range of 21–25 × 10^6 µm^2. The microstructural characterization was performed on polished cross-sections using a Zeiss Merlin FEG-SEM equipped with a backscatter (BS) detector. To fully map the work hardening that potentially takes place at the machined surfaces, both Vickers

microhardness and nanoindentations were performed. Hardness testing was carried out using Vickers microhardness measured along a line on the cross sections of the samples, from the surface to a depth of 1.6 mm with a step size of 0.12 mm. The Vickers microhardness tests were performed using a Matsuzawa MXT microhardness tester and a load of 200 g, and the nanoindentations were carried out using a Berkovich tip and a nominal depth of 100 nm. Indents were placed 2 µm apart along a line positioned at an angle (8°) to the surface tangent, beginning 30 µm into the sample and ending outside the sample (in the mounting plastic). This allowed for a controlled positioning of indents at gradually reduced depth below the sample surface.

2.5.3 Residual stress

Residual stress measurements were performed by X-ray diffraction (lab-XRD), using a Stresstech G2R XStress 3000 diffractometer equipped with a Mn X-ray tube ($\lambda = 0.21031$ nm). X-ray diffraction measures the interplanar spacing in the atomic lattice. The modified $\sin^2\chi$ method was used with ± 5 tilt (psi) angles ($45° \ldots -45°$), and the (311) lattice plane located at 151.88° was evaluated. Residual stress was calculated assuming elastic strain theory according to Hooke's law, using tabulated parameters of Young's modulus of 199.9 GPa and 0.29 for Poisson's ratio, as described by Noyan and Cohen [42]. Measurements were done in feed (building) direction and in cutting direction. Residual stress profiles were performed using layer removal using electro polishing with a Struers Movipol and Struers A2 electrolyte. All measurements were performed in an accredited laboratory in accordance with the SS-EN 15305:2008 standard [43]. The error bars in the residual stress measurements represent the error from peak fitting of the individual diffraction peaks. For the PBF-EB samples, an oscillating measurement strategy was required to suppress the strong texture.

2.5.4 Cutting tool evaluations

To study the cutting tool wear, the cutting inserts were etched in steps to remove the adhered work piece material. This was done to enable measurement of the tool wear in a more controlled way. Special attention was made to ensure the careful removal of only the adhered material by examination in the microscope during etching. The etching solution consisted of HCl (37% concentration) which was heated to a temperature of approximately 75 °C. The inserts were submerged in the heated etching solution during a total time of 1 h, with stirring of the inserts every 5 min to make sure that the adhered material came off. After the etching, some of the inserts were observed in the LOM (Zeiss Axio Zoom) to verify that the adhered material had been removed. Before observations in the SEM (Jeol 7000F), the samples were put in ethanol and cleaned by ultrasonic cleaning.

3 Results

3.1 Machining and tool wear

The samples were prepared by rough machining as described in Table 3. This machining involved tough intermittent machining and severe tool wear, e.g. chipping.

The tool wear propagation was analysed in the subsurface after finishing and showed an increasing flank- and crater wear on clearance and rake side respectively on tools used for the as-built PBF-EB. For the as-built PBF-LB material, the tool flank wear was lower on the clearance side and the coating was worn on the rake side, but no crater development. Both variants showed a clear notch at cutting depth (see Fig. 3).

Tool wear mechanisms in heat-treated components were the same as in the as-built variants. The PBF-EB showed a similar wear mechanism in both conditions, while the PFB-LB had more flank wear in the heat-treated condition but with less wear on the rake side (see Fig. 3).

The corresponding flank wear, VB_{Max}, of the inserts has been summarized in Table 4. These results show a linear increase in flank wear with cutting length except for the PBF-EB after 334.6 m which suffered from crated wear. Hence, this was replaced, and the test restarted. It is further seen that for PBF-LB, the heat-treatment increased the tool wear with 49% but only 14% for the PBF-EB. Further, PBF-EB has induced an 87% higher tool wear compared to PBF-LB for the as-built condition and 43% higher for the heat-treated condition.

3.2 Sample geometry and topography

To simplify the turning operation, rotational symmetric samples were produced for these cutting tests. However, due to the thermal heating and cooling in the printing process, the stress relief operation of the samples was distorted prior to the machining operation. The geometry was measured using 3D scanning and compared to the nominal CAD model as shown in Fig. 4. In general, the PBF-EB showed higher distortion for both conditions, the as-built and heat-treated, in comparison to the PBF-LB samples.

The topography, represented as 3D maps, shows significant differences between as-built PBF-LB and PBF-EB material (as seen in Fig. 5). This difference is also seen in the Sa and S10z parameters, which are mean values for three positions of each sample and standard deviations. The results show a 6 times higher Sa for PBF-EB, 53.7 µm, compared to the PBF-LB 8.4 µm. The corresponding S10z

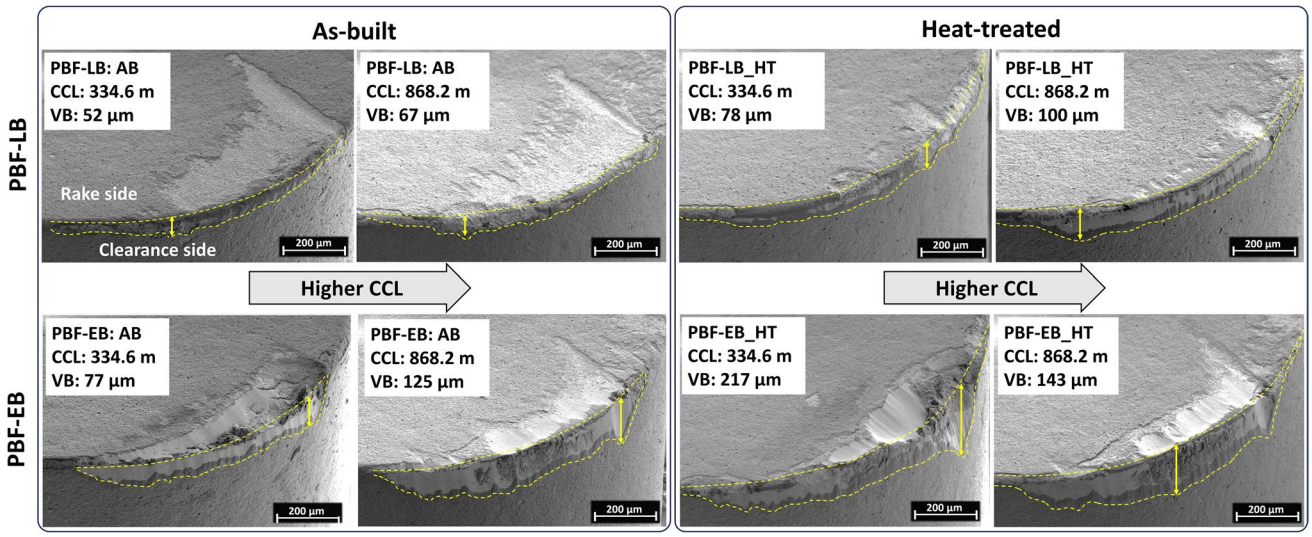

Fig. 3 SEM images in × 300 magnification of tool flank wear (VB_{Max}) propagation for as-built and heat-treated conditions of PBF-EB and PBF-LB after 334.6 and 868.2 m of cutting length

Table 4 Measured maximum tool flank wear (VB_{Max}) for the studied materials

Cutting length (m)	PBF-LB As-built (µm)	PBF-LB Heat-treated (µm)	PBF-EB As-built (µm)	PBF-EB Heat-treated (µm)
334.6	52	78	77	217*
625.6	55	92	103	125
868.2	67	100	125	143

*Insert suffered from chipping failure as seen in Fig. 3

values were 203 µm for PBF-LB and 491 µm for PBF-EB. In principle, this means that to completely remove asperities from the printing process, at least 200 µm need to be removed from the PBF-LB surface and 500 µm from the PBF-EB surface. Additionally, the Sa and S10z values show a high variation between the three measurements, shown as a high standard deviation. The two surfaces also show different surface features where the PBF-LB surface has unmelted particles while the PBF-EB surface instead shows larger flake-shaped features with a size of 0.5–1

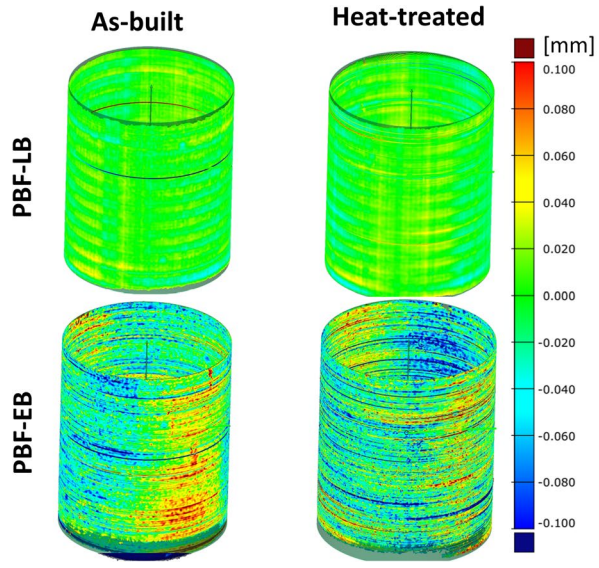

Sample	Cylindricity [mm]	Roundness [mm]
Nominal	0	0
PBF-LB, As-built	0.44	0.39
PBF-LB, Heat-treated	0.25	0.21
PBF-EB, As-built	0.76	0.52
PBF-EB, Heat-treated	0.79	0.80

Fig. 4 3D scanning analysis in respect to a nominal cylinder showing the deviation, cylindricity and roundness of the PBF-LB and PBF-EB in as-built and heat-treated samples

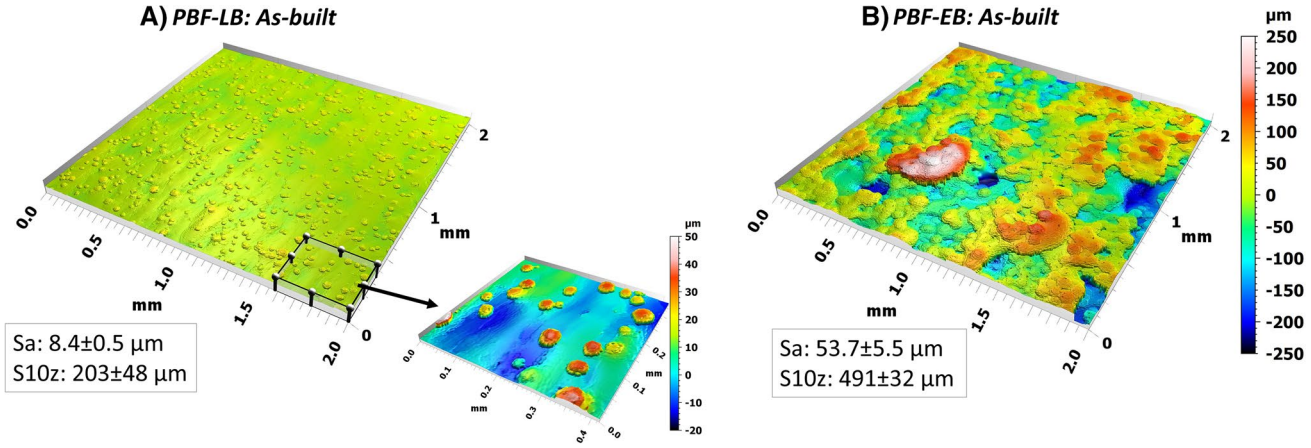

Fig. 5 3D topography maps of as-built PBF-LB (**A**) and PBF-EB (**B**) samples, before turning

mm. The topography after heat treatment, not included in Fig. 5, has similar topography values.

The topography was also evaluated as profiles from the cross sections with apparent differences as can be seen in Fig. 6. The two exemplified sections of the as-built material show an outer section consisting of protrusions and partially melted powder particles and an inner section that is completely melted. Comparing the cross-section profiles from the PBF-EB and PBF-LB samples shows an apparent difference in roughness. The PBF-EB profiles show a peak and valley structure that is not present in the PBF-LB profiles. It is also observed re-entrant features, as defined by Triantaphyllou et al. [44], linked to the peak and valley structure for the EB-PBF material, one example of which can be seen in Fig. 6B, while much smaller features are seen in the PBF-LB profiles, Fig. 6A. The protruding roughness features of the PBF-LB surface have directionality that can be described as waves in the direction of gravity within the build chamber. Such directionality is not observed in the PBF-EB profiles.

The 3D topography maps and calculated topography parameters, presented as the mean values from three measurements including the standard deviation, after finish machining are seen in Fig. 7. The results show apparent feed groves that are the main contributor to the surface roughness. The surface roughness represented by Sa is 0.3 µm for the PBF-LVB in both conditions, while the PBF-EB has higher Sa values compared to PBF-LB, especially for the as-built condition. The higher Sa for the PBF-EB may be due to higher tool wear as the cutting edge becomes blunt, as observed in the tool wear results in Fig. 3. A similar trend is observed for the S10z value. The Sdr parameter shows slightly higher values for PBF-LB in heat-treated condition and the PBF-EB in as-built condition, which implies more texture in the feed groves for these surfaces. Additionally, in the lower right of each

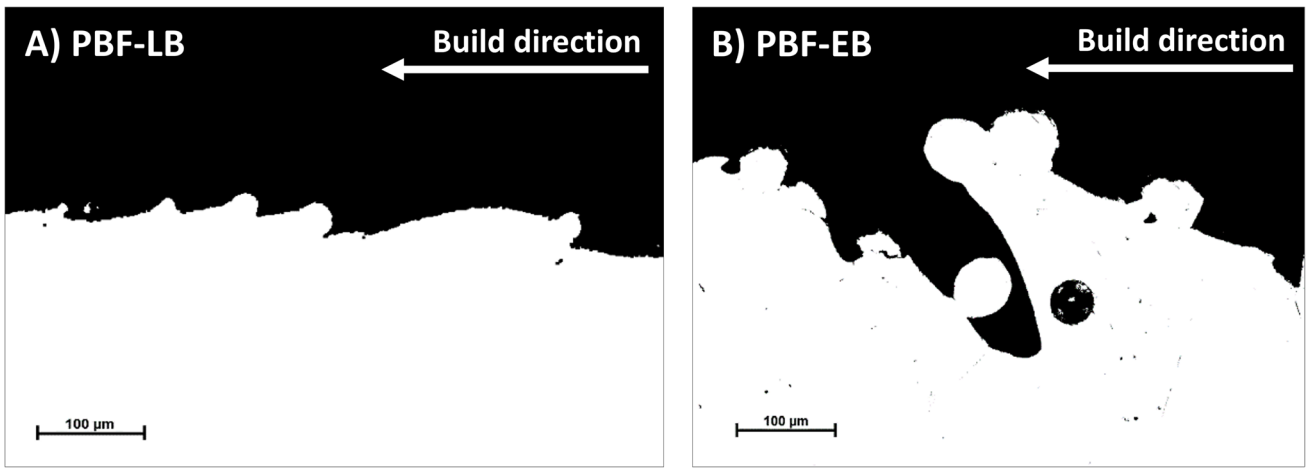

Fig. 6 Wave like features on the as-built PBF-LB sample (**A**) and Surface notch features on the as-built PBF-EB sample (**B**)

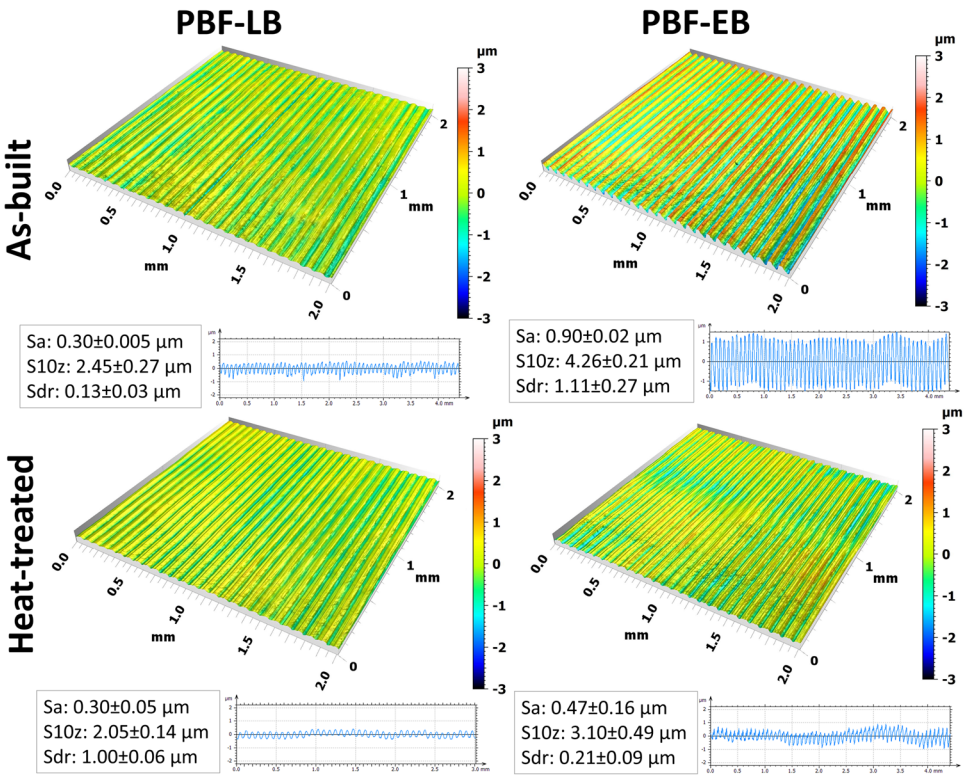

Fig. 7 3D topography images, profiles and topography parameters of PBF-LB and PBF-EB in different conditions after finish machining

condition, the mean of ten profiles is shown. This shows the difference in topography as well in terms of the depth and shape of the feed grooves. For PBF-EB, the feed groves are deeper in as-built condition compared to the heat-treated condition. The heat-treated condition further shows that the amplitude varies. The PBF-LB samples have a much lower feed groove amplitude, and the shape of the peaks is rounder, creating more of a sinusoidal shape compared to the PBF-EB peaks that are irregular. A long waviness is observed for all samples which most likely are connected to vibrations induced during machining.

3.3 Residual stresses

The surface residual stresses after the finish cut in the PBF-LB and EBP-EB samples in as-built and heat-treated condition are shown in Fig. 8. The results are the mean values for three measurement positions along the building

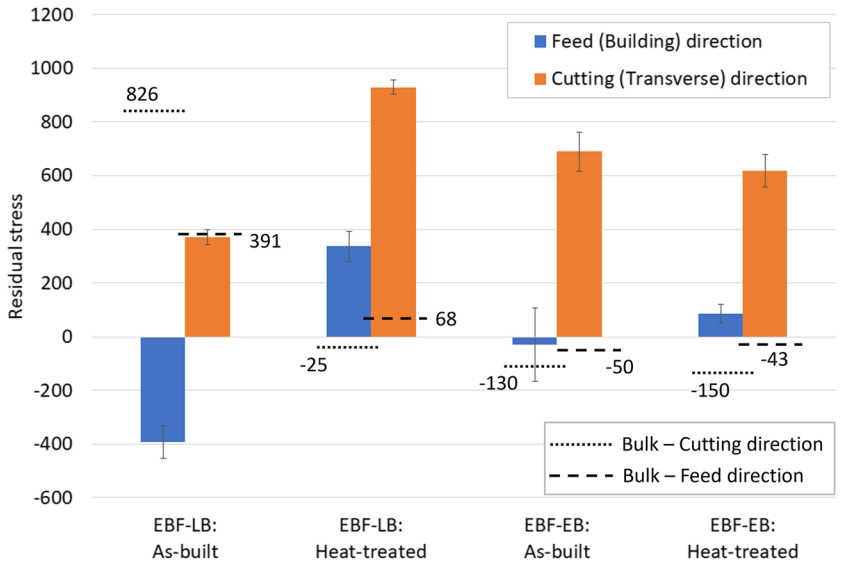

Fig. 8 Mean surface residual stresses for measurements after machining for PBF-LB and PBF-EB in as-built and heat-treated condition

direction of the samples, and the error bars represent the standard deviation for the three measurements. The dashed lines show the bulk stresses measured at a depth of 0.3 mm below the surface prior to the cutting test.

In general, the results show that turning has induced a significantly different stress condition in the samples related to the two directions, feed and cutting direction. For the as-built PBF-LB material, a moderate compressive stress is introduced in the feed (build) direction and tensile stress in the cutting direction, with a similar magnitude as the bulk prior to machining. A significant change of stresses is observed for the heat-treated material, which shows tensile stresses in both directions ranging up to 900–1000 MPa in cutting direction and a moderate tensile stress of 300–400 MPa in feed direction. In relation to the different positions, a minor difference could be seen in Fig. 8 represented by the error bars.

The corresponding surface residual stresses after machining of the PBF-EB material are low compressive stress in feed direction and high tensile stress in cutting direction for the as-built material. The heat-treated material shows low tensile stresses in feed direction and high tensile stress in cutting direction. In relation to the different positions, a greater difference is observed for the PBF-EB material as shown by the error bars. For all samples, the variation around the sample were measured showing that the stresses could vary up to 140 MPa.

The residual stress profiles for the PBF-LB and PBF-EB after turning are shown in Fig. 9. The dashed lines show bulk values measured prior to the machining operation, in the as-built and heat-treated conditions. The turning test of the PBF-LB as-built material shows a great difference between the feed and cutting direction. The cutting direction shows a superficial tensile stress that drastically drops to a

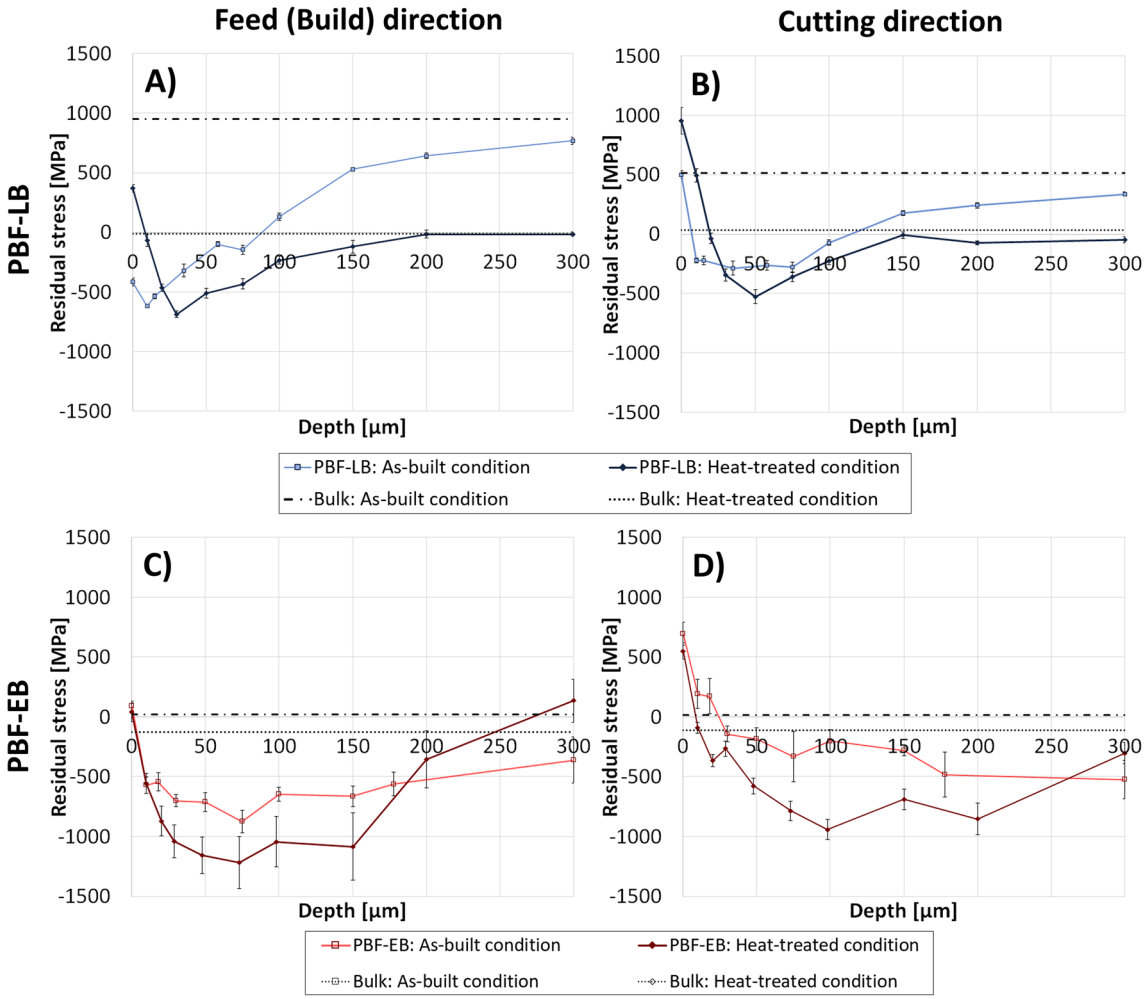

Fig. 9 Residual stress profiles after turning for as-built and heat-treated conditions of PBF-LB in feed direction (**A**), PBF-LB in cutting direction (**B**), PBF-EB in feed direction (**C**) and PBF-EB in cutting direction (**D**)

compressive stress below the surface. For both directions, a compressive zone is shown, which extends deeper for the cutting direction. At greater depth, both directions gradually become tensile, until the bulk stress condition is reached at 300 µm. Turning of PBF-LB in heat-treated condition induced high tensile stresses in the surface for both directions. The tensile stresses go into compressive stress at a depth of 10–30 µm followed by a deep compressive stress zone. The total impact depth, i.e. the depth where the bulk stresses are reached, is however lower compared to the as-built sample with an impact 150–200 µm deep.

The residual stress profiles after turning for the PBF-EB samples in as-built and heat-treated condition are shown in Fig. 9. Generally, close to the surface, it could be observed similar results, but at greater depths, the heat-treated condition has a deeper compressive stress compared to the as-built condition. It is further seen a greater variation in each measured position in the profile, seen in the error bars, which can be connected to large grains and texture in these samples. For the as-built sample, both directions have tensile surface stresses that change into compressive ones below the surface at a depth of 10–30 µm. The feed direction has a deep compressive zone, and at a depth of 300 µm, the bulk stresses are reached. However, there is a great variation in stresses at this depth for the two directions. The total affected depth is not completely covered for these measurements and is located deeper than 300 µm. Similarly, to the PBF-LB, machining of the heat-treated samples shows smoother-shaped profiles characterized by tensile stress, rather high in tangential direction. Below the surface, the stresses change into high compressive stresses with a maximum depth of 100–200 µm. It is further observed a deeper impact with greater magnitudes compared to the as-printed profiles. The total impact depth is not completely covered in these measurements, but is in the range of 200–350 µm in feed direction and greater than 300 µm in cutting direction. It is shown that stresses differ greatly at depths greater than 150 µm.

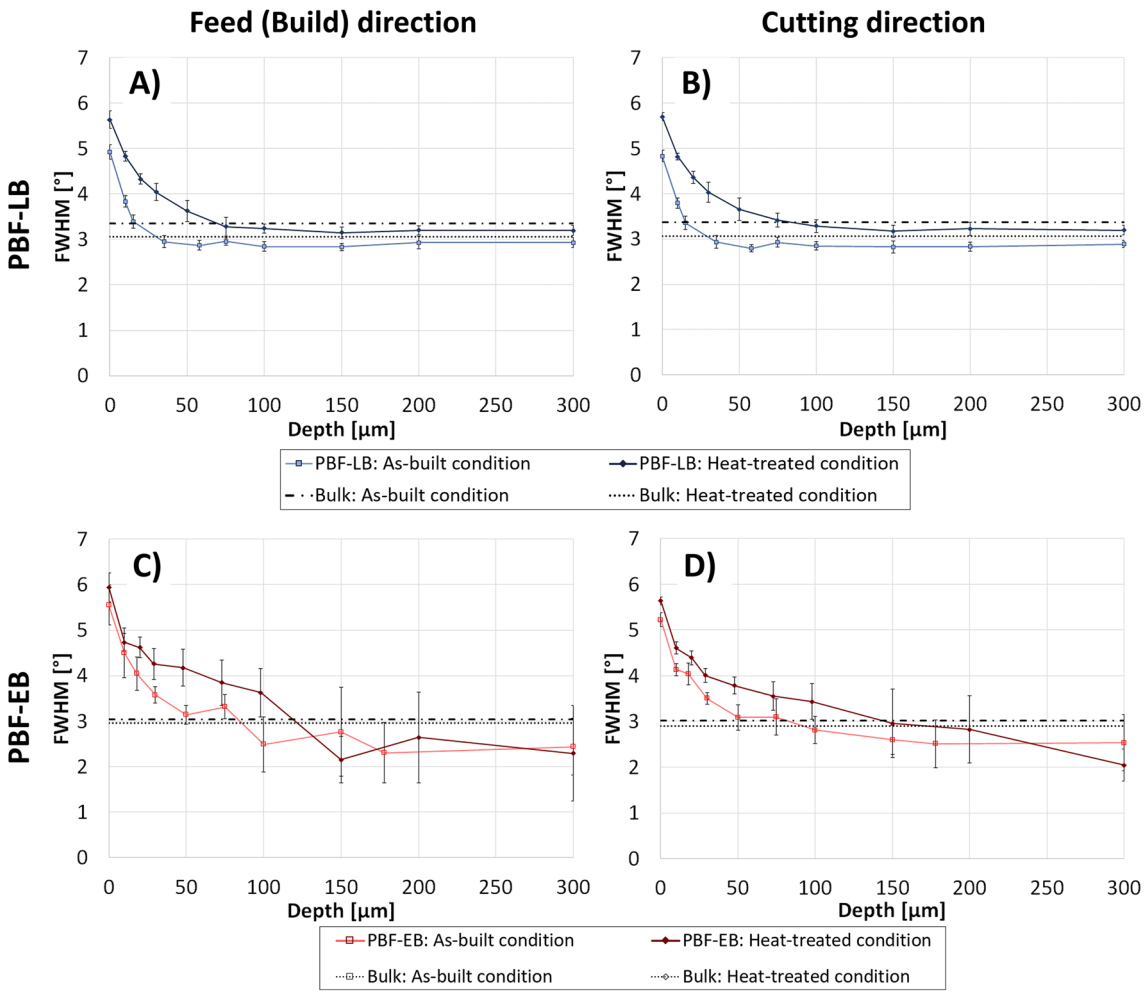

Fig. 10 Full Width Half Maximum (FWHM) profiles after turning for as-built and heat-treated conditions of PBF-LB in feed direction (**A**), PBF-LB in cutting direction (**B**), PBF-EB in feed direction (**C**) and PBF-EB in cutting direction (**D**)

The machining-induced deformation could be evaluated from the diffraction peak broadening. In Fig. 10, the connected Full Width Half Maximum profiles are shown for the PBF-LB and PBF-EB samples in the two conditions. The dashed lines show the values from prior to the machining operation. The results show a significant difference between the two materials and also between the two conditions. The profiles for PBF-LB are smoother and show a low penetration depth of 25 µm, while the heat-treated condition is 75–100 µm deep. The surface deformation is also lower for the as-built condition. The PBF-EB shows much greater variation in the profiles and a much smaller difference in the surface deformation. The penetration depth is difficult to precisely define as the profiles vary, but it is shown that the as-built material is typically around 75–100 µm, while the heat-treated condition shows a penetration depth of 125–150 µm.

3.4 Microstructure and hardness

The as-built and heat-treated microstructures were analysed in detail using Scanning electron microscopy (SEM). As shown in Fig. 11, the PBF-LB material has larger grains from the core of the specimen to the surface, whereas the PBF-EB materials contained smaller grains, especially close to the surface.

The LB-PBF material in Fig. 11A shows precipitates in the grain boundaries after printing, but no delta phase is evident. After heat-treatment of the PBF-LB material, more precipitates can be observed along the grain boundaries as shown in Fig. 11B. In contrast to the PBF-LB samples, the PBF-EB has a clearly visible printed contour with a thickness of 300–600 µm. This is observed as a zone with comparably smaller and almost equiaxed grains compared to the much larger grains elongated in the build direction in the core, not included in Fig. 11. Strain in the grains (in the PBF-EB images) is evidenced by different shades of grey within the grains. Delta phase is present, evident as large white needle-like precipitates in the grain boundaries, especially in the as-built material in Fig. 11A. After heat-treatment, the grain boundaries are increasingly more decorated with precipitates. Some strain has been relieved, and the delta phase is still present and observed as high contracts within the grains in these micrographs.

The polished cross-sections of the different samples were also used for estimations of the porosity near the surface. Table 5 shows the amount and type of porosity at different positions along the build direction for the studied materials showing higher from PBF-EB than for PBF-LB and that there are some differences at the different positions in the sample as well.

Table 5 Near surface porosity levels of the different samples at different positions in building direction

Sample	Position	Spherical porosity (%)	Irregular porosity (%)	Total porosity (%)
PBF-EB	Top	0.42	0.02	0.44
	Middle	0.42	0.26	0.63
	Bottom	0.24	0.04	0.28
PBF-LB	Top	0.1	0.03	0.13
	Middle	0.11	0.02	0.13
	Bottom	0.005	0.005	0.01

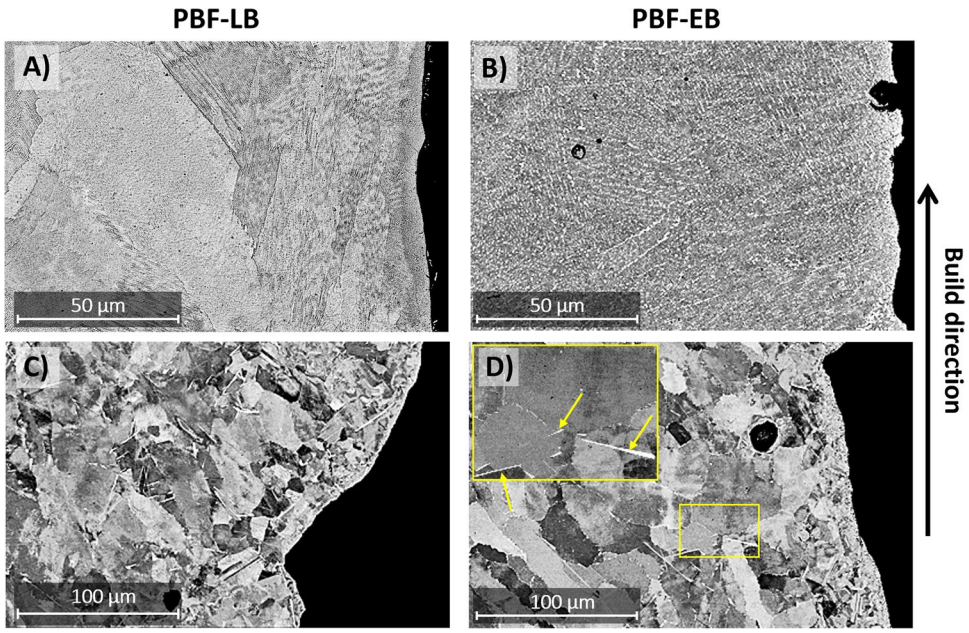

Fig. 11 Microstructure of the samples of PBF-LB: As-built (A), PBF-LB: Heat treated (**B**), PBF-EB: As-built (**C**) and PBF-EB: Heat treated (**D**), delta-phase indicated by yellow arrows

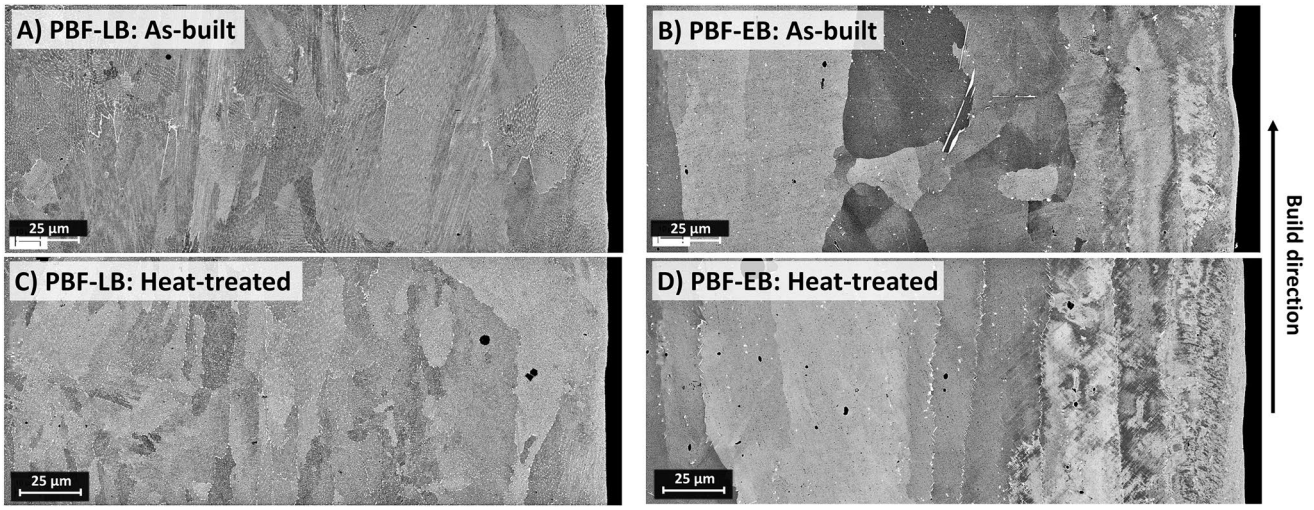

Fig. 12 Microstructure after turning for PBF-LB as-built (**A**), PBF-EB as-built (**B**), PBF-LB heat-treated (**C**) and PBF-EB heat-treated (**D**). The cut surface is on the right side of each image, and the cutting direction is perpendicular to the image plane

The impact from the turning on the microstructure is shown in Fig. 12 for PBF-LB and PBF-EB. The deformation induced in the PBF-LB sample is low, no superficial deformed layer is shown in Fig. 12, and the precipitates decorating the grain boundaries are intact and still in place all the way to the surface. After finishing the PBF-EB material, where the printed contour is completely removed, the cut surface shows both strained grains, evidenced by shades of grey within grains, to a depth of about 40 µm and a superficial layer with grain refinement. The superficial layer is very distinct and about 2 µm thick when cutting in the as-printed material and less distinct up to 10 µm thick when cutting in the heat-treated material.

The mean hardness profiles for the as-built and heat-treated conditions from measurements at different positions along the building direction of the samples are shown in Fig. 13. The error bars represent the standard deviation for the three positions. The results indicate a significant difference between the PBF-LB and the PBF-EB in the as-printed condition, whereas after heat-treatment, they possess comparable hardness values. In the as-built condition, the PBF-EB material exhibits higher hardness compared to the PBF-LB.

Nanoindentation was used to measure the hardness of superficial regions with the results as seen in Fig. 14. As both PBF-EB materials showed transformed superficial regions a few microns thick, the first region to be measured (on all samples) was at depths between 1 and 3 µm. A heavily deformed region was found on the PBF-EB samples, so the second region measured on all samples was at depths between 8 and 30 µm to capture any such region. In

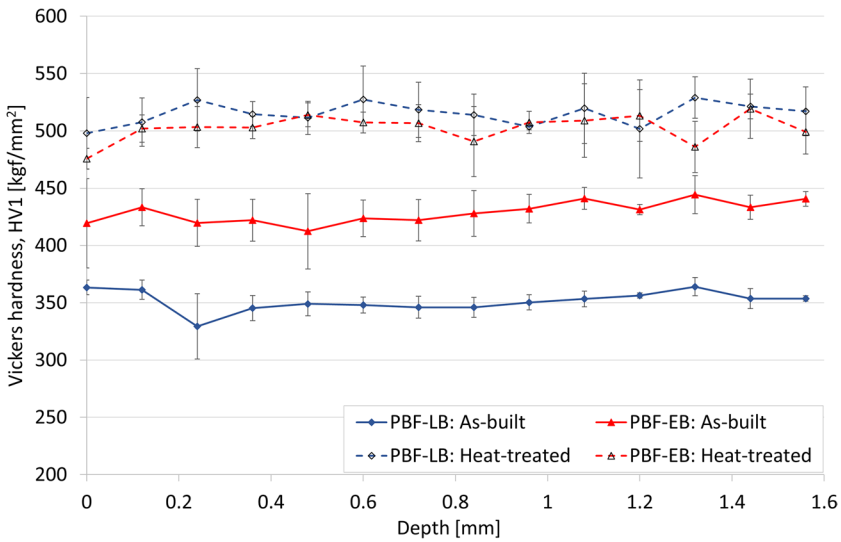

Fig. 13 Hardness profiles for PBF-LB and PBF-EB samples in as-built and heat-treated condition

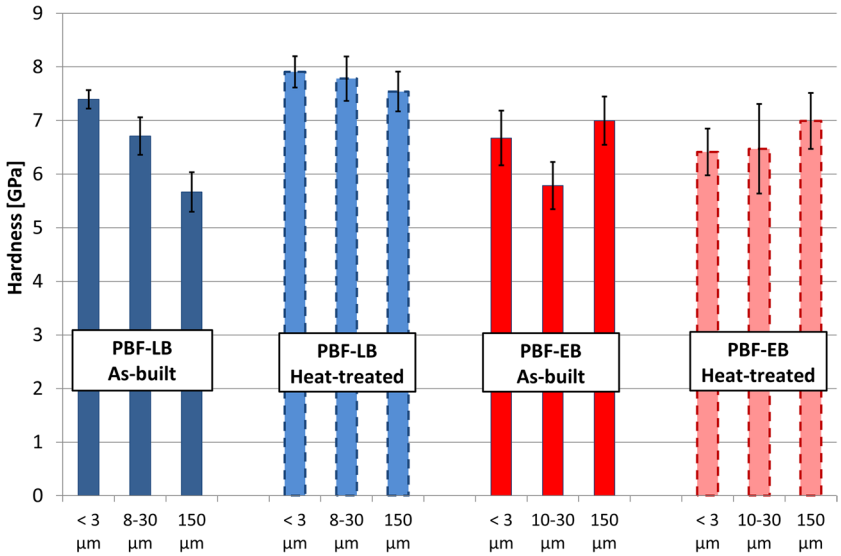

Fig. 14 Hardness measured using nanoindentation in three regions: in a surface region with possible transformed material (1–3 µm), in a region deeper than any transformed layer (8–30 µm) and deeper than any deformed layer (at 150 µm)

addition to these two regions, the hardness at a depth of 150 µm below the surface was measured. All measurements were made with a Berkovich tip and a target depth of 100 nm. All positions were confirmed, and every depth below the surface was measured in a microscope after the experiments. The values are different, but the order of the samples as measured in the deepest region corresponds to the order of the bulk Vickers hardness measurements shown in Fig. 13. It should be noted that the grain size is only slightly larger than the depth of these regions, which means the hardness levels may be influenced by differences in individual grains.

The measurements of the PBF-LB in as-built confirm that the cutting caused a significant increase in the hardness of this material, both in the outermost surface and in the intermediate region below that. In contrast, the heat-treated PBF-LB material which has a higher starting hardness has only a slight tendency to increase in hardness due to cutting. The two PBF-EB materials, as-built and heat-treated, seem to be harder in the deep region rather than in the surface region, and only the as-built material shows a tendency to have an increase in the very outermost region.

4 Discussion

4.1 Prerequisite for machining: As-built and heat-treated conditions

The two investigated AM methods in this work, PBF-LB and PBF-EB, are both employing the powder bed method, but the melting sources and process environments are entirely different. This will consequently have a great impact on topography, microstructure and residual stresses. The main contribution to the process difference is connected to how the powder melts and solidifies. The high and constant temperature of the PBF-EB printing has its main advantages in a low resulting stress after printing but on the account of grain growth and isotropic microstructure due to the long processing time at the high temperatures. PBF-LB on the other hand has a constant cooling from the building plate. However, this thermal transport will be affected throughout the building process as the distance increases, which may affect the temperature in the melt zone.

The topography of the as-built samples showed similar surface characteristics with a rough surface consisting of unmelted and partially melted particles and surface pores. Further analysis of the cross sections showed that the surface consists of two sections, an outer part consisting of protrusions and partially melted powder and an inner section which is completely melted. Between these two layers, it is common that micro defects, small radius curvatures that can act as stress concentrators, are formed, also indicated by Zhao et al. [7]. The superficial layer further showed a great difference in porosity with significantly higher amounts of pores for the PBF-EB sample compared to the PBF-LB. The full solidity of the near surface region is crucial since such pores risk being brought to the surface by machining and are more likely to contribute to fatigue failure than pores closer to the bulk of the material, as shown by Leuders et al. [45]. Porosity measurements in this work indicate that the sub-surface porosity in the PBF-EB material is at least twice as high as in the PBF-LB material. It is also interesting to note that all samples showed both spherical and non-spherical porosity according to the separation criteria used. This might indicate that both processes not only had the typical unavoidable spherical gas porosity but also process-induced

lack-of-fusion defects [46]. The PBF-EB surface notches, shown as a peak and valley structure, not observed in the PBF-LB profiles, are likely the result of incompletely filled layers as proposed by Chan et al. and Zhao et al. [6, 7]. One important feature linked to the peak and valley structure is re-entrant features. The PBF-LB profiles on the other hand showed protruding roughness have directionality that can be described as waves in the direction of gravity within the build chamber, which was not observed in the PBF-EB profiles. Such defects are especially dangerous since they have sharp corners perpendicular to the building direction that could act as stress concentration sites and could be hard to detect using non-destructive evaluation techniques [47]. Additionally, under load, it is primarily the outer section that is load carrying and any micro notches in this section will act as stress concentrators that can be detrimental to fatigue life [6]. Hence, post processing of such surface is required if it is to be used as a functional surface.

Characterisation of the as-built topography is complex since the surface is partly porous and contains a rough structure with deep pits, especially for the PBF-EB. Hence, only using the light optical scanning method might not be an adequate approach. Therefore, an evaluation of the topography was done for the cross sections where profile images were evaluated using a Matlab script simulating a needle passing over the surface of the material as created by Eriksson et al. [48]. However, the results show good correlations where the 2D evaluated cross sections showed an Ra of 33.1 ± 2.5 for PBF-EB to be compared to confocal fusion that measured Ra 34.0 ± 5.0 µm, extracted as the mean of 10 profiles across the same sample length. The corresponding values for PBF-LB were 6.9 ± 1.2 µm for 2D and 6.9 ± 0.3 µm for confocal fusion. This is in line with the work by Flys et al. [39], who also measured using the confocal fusion technique and also showed a minor mismatch between cross sections and topography measurements.

The microstructure is also greatly affected by the two AM methods. The PBF-LB shows a fine structure, while the PBF-EB material has a coarse grain structure containing hard precipitates in the grain boundaries. Heat treatment shows a slight increase of grain boundary precipitates, while instead, the hardness is greatly increased, especially for the PBF-LB material. Thus, it was observed that the impact of grain size seems to be much less than the effect of precipitates. This is concluded from the increased hardness after heat treatment increased and the higher hardness of the PBF-EB material compared to the PBF-LB.

The residual stresses induced from the two printing methods show significant differences due to the thermal history that the material has undergone during manufacturing. This has led to individual differences both in surface stresses, depth impact and magnitude of the maximal stresses below the surface. Hence, the high temperatures and a continuous thermal transport to the building plate involved for PBF-LB have induced high tensile stresses, while PBF-EB has basically released all stresses after printing as a consequence of the stress-releasing thermal treatment and cooling of the sample. The impact from the printing is also seen in the directional difference as the PBF-LB has significantly higher tensile stresses in build direction. This is also observed as a decreasing surface stress of the samples towards the building plate. In addition to recovering the dislocations, after heat treatment, the influence of precipitation and phase change/coarsening could also add up to this individual difference but will also result in releasing the high stresses of the PBF-LB sample.

4.2 Surface integrity after machining

The surface characteristics and material properties differed greatly between PBF-LB and PBF-EB in the two different conditions, which directly have an impact on the machinability. The first consideration when machining AM parts is to handle geometrical distortion from the printing and the rough nature of the as-built material. In this work, the parts were distorted due to the printing process as such but also from the relaxation of stresses during heat treatment. Distortion needs to be handled by a roughing process, which may involve intermittent machining that sets high intermittent mechanical load on the cutting edge. Additionally, the rough topography of the as-built material may be in a similar range at the depth of cut, which will also give rise to high loads on the cutting edge as the microstructure of this surface material will greatly alter with depth. In this work, two or three roughing passes were required to get rotational symmetric parts, which generated a wavy texture. This is most likely from vibrations due to inferior robustness in the tool holder of the spindle. The material properties, precipitates and residual stresses may also vary along the building direction due to the printing process as such. This is a result of the printing strategy and heat transfer to the building plate during the build, which will also have an impact on the tool wear.

Early in this work, from the roughing passes, it was concluded that the tool wear is critical to control as it determines the resulting surface integrity of the work piece material. The machining tests showed clear trends regarding the tool wear depending on the material and its condition. In the as-built condition, the coarser microstructure from large grains and higher hardness in PBF-EB induced tool wear along the edge line and flank, while the finer grained and slightly softer, hence, more ductile PBF-LB material showed mild wear on rake face. The wear progression in heat-treated materials was similar in the PBF-EB material but switched wear type in the PBF-LB material to more pronounced flank wear and less wear on

rake face. This may be explained by the large hardness increase from the heat treatment of PBF-LB as explained by Neikter et al. [49]. The hardness difference, as seen in Fig. 13, is a direct result of the grain size, amount and distribution of the precipitates, which clearly are different between the studied materials (before and after heat-treatment). The tool wear and consequently the work piece surface integrity will significantly be affected by the heat-treatment and thereof affecting the tool wear. This has previously been observed by Malakizadi et al. [21].

The rough nature of the surfaces and low dimensional accuracy of the as-built parts required rough machining to remove the outer rough surface. This processing is very interesting but difficult to study due to great variation and intermittent tool engagement. The topography of the rough machined surface showed a heavily superimposed wavy texture both in feed and cutting direction as a direct consequence of the intermittent engagement and great variation in the microstructure. The machining impact after finishing showed a great difference in the topography of the two as-built materials, where PBF-EB had three times higher Sa compared to PBF-LB. The PBF-LB showed similar roughness in the heat-treated condition, while the PBF-EB showed lowered roughness for the heat-treated condition. This implies that the as-printed PBF-EB is causing a tool wear early due to the microstructure on the surface. The difference is most likely initiated by the difference in tool wear where the more severe wear of the tools used for cutting in PBF-EB due to the higher content of the hard delta phase in the surface region of this material, results in a rougher surface. For all four materials, a long waviness could be observed, more pronounced for PBF-EB. This waviness implies vibrations during machining that might be an effect of machining in an AM microstructure with alternating distribution of grain size and participates.

In regard to the residual stresses, the differences after machining are due to the imposed deformations/strains induced by the cutting tool and work piece interaction instead of the stresses induced from the printing. In this work, x-ray diffraction was used for measurements. This is a well-established method, but it is sensitive to large grains and texture which often is the case for additively manufactured metal materials. Specific measures are needed to be developed for measurements in AM materials where oscillation strategies are used to suppress the influence of texture. This was especially the case for the EB-PBF parts for which the surface was prepared by gentle polishing followed by electro polishing in order to create a reference starting surface. The measured results are closely connected to the different microstructural features in the material that have been cut. For the PBF-LB, it is seen that the harder heat-treated material has changed from the compressive stresses into high tensile stresses in feed direction. In cutting direction, similar surface stresses are induced, but the heat-treated samples have a much higher compressive stress impact below the surface. The corresponding tool wear shows a slightly larger wear zone on the rake side but that does not explain the large difference in stresses in feed direction for the as-built and heat-treated material. Instead, hardness and dissipated heat in the cutting zone are much higher for the heat-treated sample, and thereby, the tensile stresses are induced. Additionally, the initial high tensile stresses in the as-built PBF-LB material could play a role in how easily the material is to the machine.

The residual stress profiles for the PBF-EB samples show similar levels for the two conditions with a slightly deeper impact for the heat-treated sample. Heat treatment of this material resulted in less impact on both stresses and hardness compared to PBF-LB. The difference in residual stress impact between the PBF-EB and PBF-EB material is however great and most likely connected to the large difference in microstructure.

To conclude, even with the same cutting conditions, deformation can be reached sooner or later for the different materials. Hence, the penetration depth of the stresses becomes a good indicator of the difference in machinability between the two materials to be used in future work when designing cutting tools and cutting parameters.

The main scientific contribution of this work has been to show how different printing processes and subsequent heat-treatment generate completely different microstructures, which have a great impact on the machinability and resulting surface integrity of the work material. Therefore, great care needs to be taken when selecting not only the cutting process as such but also the cutting parameters.

5 Conclusions

The resulting surface integrity after machining as well as the machining process are greatly affected by the different microstructures of the studied AM process and their subsequent heat-treatment. Herein, we also include the different amounts of grain boundary precipitates and the presence of the delta phase, which will affect the final surface quality as obtained. The following conclusions have been made.

- Prior to the machining, the surface integrity for the respective material was characterized by:
    - The PBF-LB samples showed similar, relatively low, surface roughness and high tensile stresses especially in building direction. After heat-treatment, the precipitations at the grain boundaries were further increased and the residual stresses were almost completely relaxed.

- The PBF-EB samples resulted in a similar, relatively high, surface roughness and low compressive residual stresses and showed a microstructure with delta phase and small grain boundary precipitates. After heat-treatment, the amount of grain boundary precipitates increased, which also resulted in complete stress relaxation.

- After machining, the surface integrity for the respective material was characterized by:
  - The PBF-LB material generated similar low surface roughness, but a great difference in residual stresses with moderate compressive for as-built and moderate tensile for heat-treated in feed (building), while the cutting (transverse) direction showed high tensile stresses in both conditions.
  - The PBF-EB generated an almost two times higher surface roughness for the as-built sample compared to the heat-treated conditions. The two conditions induced comparably similar surface stresses of low tensile stresses in feed (building) direction and high tensile in cutting (transverse) direction, while the residual stresses profiles showed a higher compressive stress for heat-treated material.

- As regards to the tool wear, PBF-LB material resulted in lower tool flank and crater wear as compared to the PBF-EB material, 87% higher for the as-built material and 43% higher for the heat-treated condition. The difference is attributed to the amount and distribution of hard grain boundary precipitates (higher hardness).
- In summary, the results of this work clearly show that there is a risk of unfavourable surface integrity and excessive tool wear if machining parameters for conventional materials are used for AM materials. Instead, it is recommended to adjust the machining parameters to the microstructure of the AM material.

Acknowledgements The authors would like to acknowledge the support and funding granted by the Swedish Arena for Additive Manufacturing and to Höganäs AB for supplying the powder material. Also, the Center for Additive Manufacturing—Metal (CAM2)—is acknowledged for the financial support.

Funding Open access funding provided by RISE Research Institutes of Sweden. This research has been funded by the Swedish Arena for Additive Manufacturing and Vinnova through grant ref no. 2016–05175. The researchers at Uppsala acknowledge the Swedish Foundation for Strategic Research (SSF) project GMT14-048 (Additive Manufacturing—Development of Process and Materials) and the Swedish Research Council, grant 2016–05460, for financial support.

Declarations

Competing interests The authors declare no competing interests.

References

1. Haines MP, Rielli VV, Primig S, Haghdadi N (2022) Powder bed fusion additive manufacturing of Ni-based superalloys: a review of the main microstructural constituents and characterization techniques. J Mater Sci. https://doi.org/10.1007/s10853-022-07501-4
2. Kelkar R, Andreaco A, Ott E, Groh J (2018) Alloy 718: Laser powder bed additive manufacturing for turbine applications. In: Ott E, Liu X, Andersson J, et al (eds) Proceedings of the 9th international symposium on superalloy 718 & derivatives: energy, aerospace, and industrial applications. Springer International Publishing, Cham, 53–68. https://doi.org/10.1007/978-3-319-89480-5_3
3. Ezugwu EO, Wang ZM, Machado AR (1999) The machinability of nickel-based alloys: a review. J Mater Process Technol 86:1–16. https://doi.org/10.1016/S0924-0136(98)00314-8
4. Hosseini E, Popovich VA (2019) A review of mechanical properties of additively manufactured Inconel 718. Addit Manuf 30:100877. https://doi.org/10.1016/j.addma.2019.100877
5. Tucho WM, Cuvillier P, Sjolyst-Kverneland A, Hansen V (2017) Microstructure and hardness studies of Inconel 718 manufactured by selective laser melting before and after solution heat treatment. Mater Sci Eng, A 689:220–232. https://doi.org/10.1016/j.msea.2017.02.062
6. Chan KS, Koike M, Mason RL, Okabe T (2013) Fatigue life of titanium alloys fabricated by additive layer manufacturing techniques for dental implants. Metall and Mater Trans A 44:1010–1022. https://doi.org/10.1007/s11661-012-1470-4
7. Zhao X, Rashid A, Strondl A et al (2021) Role of superficial defects and machining depth in tensile properties of electron beam melting (EBM) made Inconel 718. J Mater Eng Perform 30:2091–2101. https://doi.org/10.1007/s11665-021-05487-9
8. Frazier WE (2014) Metal additive manufacturing: a review. J Mater Eng Perform 23:1917–1928. https://doi.org/10.1007/s11665-014-0958-z
9. International Organisation for Standarization (2021) ISO/ASTM 52900:2021 Additive manufacturing—general principles—fundamentals and vocabulary. https://www.iso.org/standard/74514.html
10. Hatami S, Ma T, Vuoristo T et al (2020) Fatigue strength of 316 L stainless steel manufactured by selective laser melting. J Mater Eng Perform 29:3183–3194. https://doi.org/10.1007/s11665-020-04859-x
11. Wimler D, Käsznar K, Musi M et al (2021) How electron beam melting tailors the Al-sensitive microstructure and mechanical response of a novel process-adapted γ-TiAl based alloy. Mater Des 212:110187. https://doi.org/10.1016/j.matdes.2021.110187

12. Deng D, Peng RL, Brodin H, Moverare J (2018) Microstructure and mechanical properties of Inconel 718 produced by selective laser melting: sample orientation dependence and effects of post heat treatments. Mater Sci Eng, A 713:294–306. https://doi.org/10.1016/j.msea.2017.12.043
13. Wang X, Gong X, Chou K (2017) Review on powder-bed laser additive manufacturing of Inconel 718 parts. Proc Inst Mech Eng, Part B: J Eng Manuf 231:1890–1903. https://doi.org/10.1177/0954405415619883
14. Stavropoulos P, Foteinopoulos P, Papacharalampopoulos A, Bikas H (2018) Addressing the challenges for the industrial application of additive manufacturing: towards a hybrid solution. Int J Lightweight Mater Manuf 1:157–168. https://doi.org/10.1016/j.ijlmm.2018.07.002
15. Zhang C, Zou D, Mazur M, et al (2023) The state of the art in machining additively manufactured titanium alloy Ti-6Al-4V. Materials 16 (7):2583. https://doi.org/10.3390/ma16072583
16. Abeni A, Loda D, Özel T, Attanasio A (2020) Analytical force modelling for micro milling additively fabricated Inconel 625. Prod Eng Res Devel 14:613–627. https://doi.org/10.1007/s11740-020-00980-x
17. Fei J, Liu G, Patel K, Özel T (2020) Effects of machining parameters on finishing additively manufactured nickel-based alloy Inconel 625. J Manuf Mater Process 4 (2):32. https://doi.org/10.3390/jmmp4020032
18. Patel K, Fei J, Liu G, Özel T (2019) Milling investigations and yield strength calculations for nickel alloy Inconel 625 manufactured with laser powder bed fusion process. Prod Eng Res Devel 13:693–702. https://doi.org/10.1007/s11740-019-00922-2
19. Yang L, Patel KV, Jarosz K, Özel T (2020) Surface integrity induced in machining additively fabricated nickel alloy Inconel 625. Procedia CIRP 87:351–354. https://doi.org/10.1016/j.procir.2020.02.104
20. Parida AK, Maity K (2018) Comparison the machinability of Inconel 718, Inconel 625 and Monel 400 in hot turning operation. Eng Sci Technol, an Int J 21:364–370. https://doi.org/10.1016/j.jestch.2018.03.018
21. Malakizadi A, Hajali T, Schulz F et al (2021) The role of microstructural characteristics of additively manufactured alloy 718 on tool wear in machining. Int J Mach Tools Manuf 171:103814. https://doi.org/10.1016/j.ijmachtools.2021.103814
22. Pérez-Ruiz JD, de Lacalle LNL, Urbikain G et al (2021) On the relationship between cutting forces and anisotropy features in the milling of LPBF Inconel 718 for near net shape parts. Int J Mach Tools Manuf 170:103801. https://doi.org/10.1016/j.ijmachtools.2021.103801
23. Chen L, Xu Q, Liu Y et al (2021) Machinability of the laser additively manufactured Inconel 718 superalloy in turning. Int J Adv Manuf Technol 114:871–882. https://doi.org/10.1007/s00170-021-06940-8
24. Taşcıoğlu E, Kaynak Y, Sharif S et al (2022) Machining-induced surface integrity of Inconel 718 alloy fabricated by powder bed fusion additive manufacturing under various laser processing parameters. Mach Sci Technol 26:49–71. https://doi.org/10.1080/10910344.2021.1998107
25. Kaynak Y, Tascioglu E (2018) Finish machining-induced surface roughness, microhardness and XRD analysis of selective laser melted Inconel 718 alloy. Procedia CIRP 71:500–504. https://doi.org/10.1016/j.procir.2018.05.013
26. Ducroux E, Fromentin G, Viprey F et al (2021) New mechanistic cutting force model for milling additive manufactured Inconel 718 considering effects of tool wear evolution and actual tool geometry. J Manuf Process 64:67–80. https://doi.org/10.1016/j.jmapro.2020.12.042
27. De Bartolomeis A, Newman ST, Jawahir IS, et al (2021) Future research directions in the machining of Inconel 718. J Mater Process Technol 297:117260. https://doi.org/10.1016/j.jmatprotec.2021.117260
28. Oyelola O, Crawforth P, M'Saoubi R, Clare AT (2016) Machining of additively manufactured parts: implications for surface integrity. Procedia CIRP 45:119–122. https://doi.org/10.1016/j.procir.2016.02.066
29. Arunachalam RM, Mannan MA, Spowage AC (2004) Surface integrity when machining age hardened Inconel 718 with coated carbide cutting tools. Int J Mach Tools Manuf 44:1481–1491. https://doi.org/10.1016/j.ijmachtools.2004.05.005
30. Arunachalam R, Mannan MA (2000) Machinibility of nickel-based high temperature alloys. Mach Sci Technol 4:127–168. https://doi.org/10.1080/10940340008945703
31. Jindal PC, Santhanam AT, Schleinkofer U, Shuster AF (1999) Performance of PVD TiN, TiCN, and TiAlN coated cemented carbide tools in turning. Int J Refract Metal Hard Mater 17:163–170. https://doi.org/10.1016/S0263-4368(99)00008-6
32. Cantero JL, Díaz-Álvarez J, Miguélez MH, Marín NC (2013) Analysis of tool wear patterns in finishing turning of Inconel 718. Wear 297:885–894. https://doi.org/10.1016/j.wear.2012.11.004
33. Sharman ARC, Hughes JI, Ridgway K (2006) An analysis of the residual stresses generated in Inconel 718™ when turning. J Mater Process Technol 173:359–367. https://doi.org/10.1016/j.jmatprotec.2005.12.007
34. Olovsjö S, Wretland A, Sjöberg G (2010) The effect of grain size and hardness of wrought alloy 718 on the wear of cemented carbide tools. Wear 268:1045–1052. https://doi.org/10.1016/j.wear.2010.01.017
35. Madariaga A, Kortabarria A, Hormaetxe E et al (2016) Influence of tool wear on residual stresses when turning Inconel 718. Procedia CIRP 45:267–270. https://doi.org/10.1016/j.procir.2016.02.359
36. Careri F, Umbrello D, Essa K et al (2021) The effect of the heat treatments on the tool wear of hybrid additive manufacturing of IN718. Wear 470–471:203617. https://doi.org/10.1016/j.wear.2021.203617
37. Pauzon C, Raza A, Hryha E, Forêt P (2021) Oxygen balance during laser powder bed fusion of alloy 718. Mater Des 201:109511. https://doi.org/10.1016/j.matdes.2021.109511
38. Townsend A, Senin N, Blunt L et al (2016) Surface texture metrology for metal additive manufacturing: a review. Precis Eng 46:34–47. https://doi.org/10.1016/j.precisioneng.2016.06.001
39. Flys O, Berglund J, Rosen B-G (2020) Using confocal fusion for measurement of metal AM surface texture. Surf Topogr Metrol Prop 8:024003. https://doi.org/10.1088/2051-672x/ab84c3
40. International Organisation for Standarization (2012) ISO 25178–2:2012, Geometrical product specifications (GPS)--surface texture: areal--part 2: terms, definitions and surface texture parameters. https://www.iso.org/standard/42785.html
41. (2018) ATOS Professional 2018-user handbook
42. Noyan IC, Cohen JB (1987) Residual stress measurement by diffraction and interpretation, 1987th edn. Springer-Verlag, New York Inc
43. European Committee for Standardization (2008) EN 15305:2008 E, Non-destructive testing–test method for residual stress analysis by X-ray diffraction. https://www.enstandard.eu/bs-en-15305-2008-non-destructive-testing-test-method-for-residual-stress-analysis-by-x-ray-diffraction/
44. Triantaphyllou A, Giusca CL, Macaulay GD et al (2015) Surface texture measurement for additive manufacturing. Surf Topogr Metrol Prop 3:024002. https://doi.org/10.1088/2051-672x/3/2/024002
45. Leuders S, Vollmer M, Brenne F et al (2015) Fatigue strength prediction for titanium alloy TiAl6V4 manufactured by selective laser melting. Metall and Mater Trans A 46:3816–3823. https://doi.org/10.1007/s11661-015-2864-x
46. Hrabe N, Gnäupel-Herold T, Quinn T (2017) Fatigue properties of a titanium alloy (Ti–6Al–4V) fabricated via electron beam melting (EBM): effects of internal defects and residual stress. Int J Fatigue 94:202–210. https://doi.org/10.1016/j.ijfatigue.2016.04.022

47. Sandell V, Hansson T, Forsberg F, et al (2020) X-ray micro tomography study of internal defects of electron beam melted Ti6Al4V and their effect on fatigue behavior. MATEC Web Conf 321:03029. https://doi.org/10.1051/matecconf/202032103029
48. Eriksson R, Sjöström S, Brodin H et al (2013) TBC bond coat–top coat interface roughness: influence on fatigue life and modelling aspects. Surf Coat Technol 236:230–238. https://doi.org/10.1016/j.surfcoat.2013.09.051
49. Neikter M, Raja DC, Balachandramurthi AR, Harlin P (2021) Tailored ductility and strength for enhanced impact toughness of laser powder fusion built alloy 718. J Alloy Compd 884:161374. https://doi.org/10.1016/j.jallcom.2021.161374